Journal of Materials Chemistry A

ROYAL SOCIETY OF CHEMISTRY

PAPER

View Article Online
View Journal | View Issue

Check for updates

Cite this: *J. Mater. Chem. A*, 2024, **12**, 7257

Correction and new understanding of the reactivity of illuminated tungsten trioxide in the dark: antecedents and consequences of photo-storage electrons triggering Fenton reactions†

Hao Huang, Hui-Long Wang * and Wen-Feng Jiang*

Received 12th December 2023
Accepted 8th February 2024

DOI: 10.1039/d3ta07689j

rsc.li/materials-a

Water treatment *via* photocatalytic steps is severely constrained by the alternation of day and night and the shading of sunlight by clouds. As an energy storage photocatalyst, WO_3 has been reported to function partially even under dark conditions, which is of great significance for the construction of round-the-clock photocatalysts. However, pertinent reaction processes, especially the function of stored electrons in WO_3 during catalytic reactions in the dark, have not been fully analyzed. Herein, we synthesized hexagonal WO_3 hydrate (h-$WO_3 \cdot 0.46H_2O$) and used extensive experiments and theoretical calculations to investigate its structure, photochromic capability, and dark reaction activity. Due to the strong interaction between the protons from lattice water and bridging oxygen atoms (W–O–W), h-$WO_3 \cdot 0.46H_2O$ exhibited unexpected irreversible photochromic properties under visible light. Our study is the first to show that light-irradiated h-$WO_3 \cdot 0.46H_2O$ can activate H_2O_2 to form $^{\bullet}O_2^-$, $^{\bullet}OH$, and $^1O_2$, which are responsible for the efficient degradation of organic pollutants, but it could not produce reactive oxygen species (ROS) *via* the $1e^-/2e^-$ ORR in the dark. This study not only provides a novel and inexpensive Fenton catalyst for wastewater treatment, but also proposes a new approach for utilizing solar energy under dark conditions.

1 Introduction

Significant water contamination issues have been brought about by the widespread use and unreasonable discharge of organic compound products such as dyes, insecticides, and personal care items.[1–3] These organic pollutants pose a major hazard to human health, since they are not only extensively dispersed but also extremely poisonous. Photocatalytic technology is considered the most effective technique for environmental rehabilitation by eliminating the aforementioned organic contaminants owing to its simplicity of use, low cost, and absence of secondary contamination compared to conventional water treatment technologies (*e.g.* adsorption, flocculation, and advanced oxidation.[4–8]). However, the presence of diurnal alternation and the shading of sunlight by clouds under natural conditions severely limits the utilization of sunlight for semiconductor photocatalysis and makes the photocatalytic reaction time-limited in practical applications.[9,10] Therefore, it is of great importance to find materials that can effectively store solar energy and continue catalytic reactions in the dark to achieve full utilization of solar energy and round-the-clock photocatalytic reactions.

WO_3 is considered promising for the storage of solar energy and round-the-clock photocatalytic reactions owing to the reversible cycle of W^{6+}/W^{5+}. The reported mechanism can be represented by eqn (1) and (2), where M stands for H or alkali metals.[11,12]

$$WO_3 + xe^- \text{ (CB)} + xM^+ \rightarrow M_xW^{5+}{}_xW^{6+}{}_{1-x}O_3 \text{ (charging)} \quad (1)$$

$$M_xW^{5+}{}_xW^{6+}{}_{1-x}O_3 \rightarrow WO_3 + xe^- + xM^+ \text{ (discharging)} \quad (2)$$

Based on the reversible structural transformation described above, many research studies on the degradation of organic pollutants by round-the-clock photocatalysts containing WO_3 have been reported (Table S1†). Although WO_3 exhibits obvious storage properties for photogenerated electrons and many studies have been reported on its properties and mechanisms for round-the-clock catalytic degradation of pollutants, there are still several issues that have not been fully addressed. Firstly, the limited storage capacity of photogenerated electrons and the rapid release of stored electrons lead to shorter catalytic reaction times under dark conditions. Secondly, low catalytic reaction activity under dark conditions cannot be matched with that under light illumination. Most importantly, the mechanism of catalytic reactions under dark conditions is ambiguous.

School of Chemistry, Dalian University of Technology, Dalian 116023, China. E-mail: hlwang@dlut.edu.cn; dlutjiangwf@163.com

† Electronic supplementary information (ESI) available. See DOI: https://doi.org/10.1039/d3ta07689j

For most reported dark reaction mechanisms of WO_3-based round-the-clock photocatalysts in the absence of light, the degradation of organic pollutants in the dark is attributed to the formation of ·OH (decomposition of H_2O_2 formed by the oxygen reduction reaction) or $^{\cdot}O_2^-$ through the oxygen reduction reaction (ORR) by stored electrons (Table S1†). It is worth noting that the electrons stored in WO_3 may reduce oxygen molecules under dark conditions through the following possible pathways (eqn (3)–(7)):[13–15]

$$O_2 + e_{CB}^- \rightarrow {}^{\cdot}O_2^- \; E^{\circ} = -0.33 \; V_{NHE} \quad (3)$$

$$^{\cdot}O_2^- + H^+ \rightarrow {}^{\cdot}OOH \quad (4)$$

$$^{\cdot}OOH + H^+ + e_{CB}^- \rightarrow H_2O_2 \; E^{\circ} = +1.44 \; V_{NHE} \quad (5)$$

$$O_2 + 2e_{CB}^- + 2H^+ \rightarrow H_2O_2 \; E^{\circ} = +0.68 \; V_{NHE} \quad (6)$$

$$O_2 + 4e_{CB}^- + 4H^+ \rightarrow 2H_2O \; E^{\circ} = +1.23 \; V_{NHE} \quad (7)$$

It is worth mentioning that WO_3 is a typical oxidation type semiconductor with a more positive conduction band (CB) position (>0 V_{NHE}).[16–20] So, the photogenerated electrons stored in the CB of WO_3 cannot reduce O_2 to $^{\cdot}O_2^-$ ($E^{\circ} = -0.33$ V_{NHE}) from a thermodynamic point of view, and therefore there is no way to produce H_2O_2 *via* eqn (4) and (5). Although the potential of the concerted two-electron oxygen reduction reaction (concerted $2e^-$ ORR, eqn (6)) seems to be appropriate, the four-electron ORR to H_2O (eqn (7)) is thermodynamically more favourable because the electrode potential of the $4e^-$ ORR (+1.23 V_{NHE}) is more positive than that of the concerted $2e^-$ ORR (+0.68 V_{NHE}). Obviously, in order to achieve the performance of WO_3 with photo-stored electrons to degrade pollutants in the dark matching that under light illumination, it is necessary to clarify the active species production and catalytic mechanism in the absence of light.

Herein, we synthesized a crystalline hexagonal WO_3 hydrate by a simple oil-bath heating method, which exhibited excellent and stable photogenerated electron storage capacity. In addition to the conversion of W(VI) to W(V) in hexagonal WO_3 hydrate under light illumination, the lattice water molecules stored in the intracrystalline tunnels undergo splitting. The generated protons will then interact strongly with the bridging oxygen atoms in the structure, changing the colour of the hexagonal WO_3 hydrate from white to blue, which can remain stable in the atmosphere for a long time (>24 h). In contrast to the results reported in the literature, we verified that the discoloured hexagonal WO_3 hydrate could not reduce O_2 molecules to reactive oxygen species (ROS) *via* the single-electron pathway or two-electron pathway. Interestingly, the electrons stored in the light-irradiated hexagonal WO_3 hydrate, however, can significantly activate H_2O_2 in the dark, generating ROS ($^{\cdot}O_2^-$, $^1O_2$ and $^{\cdot}OH$) for the efficient degradation of organic pollutants under dark conditions. When dark-Fenton reaction (DFR) is completed, the blue hydrated WO_3 can regain its original colour and then be recycled for the next catalytic reaction process.

2 Experimental

2.1. Materials

Sodium tungstate dihydrate ($Na_2WO_4 \cdot 2H_2O$) was obtained from Energy Chemical Reagent Co., Ltd. Concentrated hydrochloric acid (37%, HCl) and polyvinylpyrrolidone with a molecular weight of 24 000 (PVP, $M = 24$ K) were purchased from Tianjin Kermel Chemical Reagent Co., Ltd .2 *sec*-Butyl-4,6-dinitrophenol (DNBP) was obtained from Aladdin Reagent Co., Ltd In addition, deionized water was used in all the operations. All reagents were used as received without further purification.

2.2. Synthesis of samples

2.2.1. Synthesis of hexagonal WO_3 hydrate. The hexagonal WO_3 hydrate was synthesized by a simple oil-bath heating method. Typically, 2 g of $Na_2WO_4 \cdot 2H_2O$ was added to a 100 ml beaker with 30 ml of deionized water and dissolved under continuous magnetic stirring. Then, 10 ml of aqueous solution containing 15 mg of PVP was added dropwise to the above solution and kept stirring for 5 min. After that, 1.5 mmol Na_2SO_4 was poured into the above transparent solution and stirred for 30 min to dissolve it. The system was then heated to 90 °C in an oil bath and kept warm for 10 min. Subsequently, about 4.5 ml of 3.0 M HCl solution was added dropwise to the reaction system to adjust the acidity value to 2 and the reaction was continued at 90 °C for 3 h. Finally, the obtained white product was washed 4 times with deionized water, freeze-dried, and named h-$WO_3 \cdot xH_2O$.

2.2.2. Synthesis of illuminated hexagonal WO_3 hydrate. 80 mg of h-WO_3 hydrate was dispersed into 30 ml of deionized water and kept stirring for t min under visible light irradiation (λ > 420 nm). Upon illumination, the colour of h-WO_3 hydrate gradually changed from white to blue. Then, the obtained blue precipitate was collected after centrifugation, washing and lyophilization. The final light irradiated product was named LP-t min, where t represents different light irradiation times.

2.3. Characterization

A JEM-F200 field emission transmission electron microscope (TEM) and Rigaku D/Max 2400 diffractometer equipped with monochromatized Cu Kα radiation ($l = 0.15406$ nm) were used to investigate the morphology and structures of the materials. Fourier transform infrared (FTIR) spectra were obtained with a Thermo Nicolet Avatar 360 Fourier transform infrared spectrometer. The chemical state of the elements was determined using a Thermo Fisher ESCALAB Xi^+ X-ray photoelectron spectrometer (XPS) equipped with a scanning range of 100–4000 eV, a 180° double-focusing hemispherical analyzer with a 128-channel detector, and an Al Kα micro-focused X-ray source. The optical absorption performances and optical band gap of the samples were obtained using a HITACHI U-3900 spectrometer, and $BaSO_4$ served as a standard reference substance. Electron paramagnetic resonance spectroscopy (EPR) was recorded on a Bruker A200 spectrometer at room temperature. The internal structure of the samples was investigated using a confocal

Raman spectrometer (Raman, LabRAM HR Evolution, Horiba, France) with the scanning range of 100–1000 cm^{-1}. HP6890GC/5973MSD apparatus was employed to analyze intermediate products in the degradation of the target pollutant DNBP by gas chromatography-mass spectrometry (GC-MS) mode.

Additionally, temperature programmed desorption (TPD) curves were recorded on a TGA8000-Frontier-Clarus SQ8T instrument at a heating rate of 10 °C min^{-1} in Ar. The heating range is room temperature-700 °C. The mass loss of the sample above 100 °C was ascribed to the wastage of the lattice water molecules.[21] So, the amount of lattice H_2O per WO_3 formula unit (x) can be calculated by eqn (8):

$$x = n_{H_2O}/n_{WO_3} = (m_0A_2/A_1M_{WO_3})/(m_0(A_1 - A_2)/A_1M_{H_2O}) = [(A_1 - A_2)M_{WO_3}] \quad (8)$$

wherein n_{H_2O}, n_{WO_3}, m_0, A_1, A_2, M_{WO_3} and M_{H_2O} refer to the number moles of lattice H_2O molecules present in a certain mass of $WO_3 \cdot xH_2O$ (mol), the number moles of WO_3 present in a certain mass of $WO_3 \cdot xH_2O$ (mol), a certain mass of $WO_3 \cdot xH_2O$ (g), the mass ratio of the sample above 100 °C (%), the mass ratio of the sample above the temperature (400–550 °C) at a stable mass (%), the molar mass of WO_3 (g mol^{-1}) and the molar mass of H_2O (g mol^{-1}), respectively.

2.4. Quantitative experiments on stored electrons in LP-*t* min samples and the oxidation experiments of I^- for different systems

The detailed procedures are shown in the ESI (Text S1.1 and Text S1.2).†

2.5. Theoretical calculations

Information on theoretical calculations is shown in ESI (Text S1.3).†

2.6. Performance evaluation of catalysts

The removal experiments of pollutants by the synthesized samples were carried out on a CEL-LAB500 photoreactor (CEAULIGHT Co., Ltd) equipped with a 500 W Xe lamp with a 420 nm cut-off filter. The average light intensity over the duration of each experiment was measured to be 80 mW cm^{-2}. DNBP, a typical dinitrophenol compound which is widely used in the petrochemical industry and agriculture, was chosen as a target organic contaminant. Typically, 30 mg of the as-synthesized catalyst was dispersed into 30 ml of the target pollutant solution (20 mg L^{-1}) in a quartz tube. Prior to turning on the light, the suspension was stirred in the darkness for 30 min to establish adsorption–desorption equilibrium. The system was then subjected to visible light irradiation under magnetic stirring. Samples of 3 ml were withdrawn at different time intervals, and centrifuged and the supernatant was analysed for evolution in concentration of DNBP spectrophotometrically at λ_{max} of 376 nm. The dark Fenton-like reaction (DFR) of the samples was triggered after photocatalytic experiments in the same setup. After turning off the light, 150 μL of H_2O_2 solution (10 wt%) was added into the quartz tube and kept stirring. Afterwards, the variation of DNBP concentration was monitored by the same method and procedure as described above for photocatalysis measurements. In particular, the DFR process was performed under completely dark conditions.

2.7. Electrochemical measurements

All electrochemical measurements were performed on an electrochemical workstation (Chenhua CHI 660E, Shanghai Chenhua Instrument Co., Ltd) equipped with a standard three-electrode system. Mott–Schottky (MS) measurements were performed with the same setup at a frequency of 1000/2000/3000 Hz with an amplitude of 5 mV. Linear sweep voltammetry (LSV) was performed through a rotating ring disk electrode (RRDE) with a Pt ring electrode in O_2-saturated solution, and the working electrode was prepared by loading the catalyst on a glassy carbon electrode. The number of electrons (n) transferred during the dark reaction can be calculated using the following equation:

$$n = (4 \times I_D)/(I_D + I_R/N) \quad (9)$$

wherein I_D, I_R and N refer to the disk current (mA), the ring current (mA) and the collection efficiency (0.37), respectively. In addition, the number (n) of electron transfer involved in the overall O_2 reduction was also calculated from the linear regression of the Koutecky–Levich (K–L) plot using the following equations (eqn (10) and (11)):

$$1/j = 1/j_d + 1/j_k = B^{-1}\omega^{-1/2} + j_k^{-1} \quad (10)$$

$$B = 0.2nFv^{-1/6}CD^{2/3} \quad (11)$$

where j is the current density (mA cm^{-2}), j_d is the diffusion-limited current, j_k is the kinetic current density, ω is the angular velocity of the disk electrode (rpm), v is the kinetic viscosity of water (0.01 cm^2 s^{-1}), C is the concentration of dissolved O_2 in water (1.26×10^{-3} mol L^{-1}), and D is the diffusion coefficient of dissolved O_2 (2.7×10^{-5} cm^2 s^{-1}).

All measurements were performed with the same setup in 30 ml Na_2SO_4 solution (0.5 M). The experiments were carried out at ambient temperature (25.0 ± 0.5 °C).

3 Results and discussion

The apparent morphology and microstructure of the samples were further characterized by SEM and TEM measurements (Fig. S1† and 1a). It can be clearly seen that the h-WO_3 hydrate sample shows a nano-strip morphology with a length of ~100 nm and a width of ~20 nm. The fast Fourier transform (FFT) of the HRTEM image with the lattice plane intensity profile (inset of Fig. 1b) exhibited an interplanar spacing of 0.39 nm clearly, which can be ascribed to the (001) plane of hexagonal WO_3. Additionally, the results from the selected area electron diffraction (SAED) technique (Fig. 1c) showed that the h-WO_3 hydrate sample had a splendid crystal structure with planes (100), (002), (200), and (202) of hexagonal WO_3. As shown in Fig. 1d–g, the surface of the h-WO_3 hydrate sample is uniformly distributed with O, Na and W, wherein the Na

element comes from $Na_2WO_4 \cdot 2H_2O$. On the side, the crystallographic information of the sample was obtained through powder X-ray diffraction (PXRD) analysis. The main peaks were observed at 13.96°, 22.72°, 24.33°, 26.85°, 28.17°, 33.58°, 36.57°, 49.96°, 55.33° and 55.51° (Fig. 1h), which, respectively, corresponded to Bragg reflections from the (100), (001), (110), (101), (200), (111), (201), (220), (202) and (221) crystalline planes of hexagonal WO_3 (space group $P6/mmm$),[22,23] which was consistent with the SAED findings. Thermogravimetric analysis (TGA) revealed that the mass loss of the sample above 100 °C was about 3.47% (Fig. 1i), indicating the presence of $0.46H_2O$ ($x = 0.46$) per WO_3 formula unit (calculation details are shown in Text 2.3). Based on the above results, the crystallographic structure of the prepared h-$WO_3 \cdot 0.46H_2O$ was refined (Fig. 1h), and the Rietveld refinement data are summarized in Table S2.† In h-$WO_3 \cdot 0.46H_2O$, the lattice water molecules are in the dodecagon tunnels along the z axis and reside between W–O layers along the z axis (Fig. 1j, S2a and b†).

The photochromic response of h-$WO_3 \cdot 0.46H_2O$ was investigated under continuous visible light illumination using a 500 W Xe lamp equipped with a filter (>420 nm) for different irradiation times. As shown in Fig. S3,† h-$WO_3 \cdot 0.46H_2O$ gradually changed from milky white to dark blue with the increase of illumination time. The photochromic process proceeded slowly and the color of the sample hardly changed significantly after 80 min of irradiation. This phenomenon can also be confirmed by the absorbance and reflectance spectra of different illuminated h-$WO_3 \cdot 0.46H_2O$ samples (Fig. 2a and S4†). The absorbance and reflectance of visible light area for h-$WO_3 \cdot 0.46H_2O$ underwent a significant enhancement with the increase of illumination time. Compared with the sample LP-80 min, the absorbance and reflectance of the sample LP-100 min were hardly enhanced significantly, indicating that the photochromism of h-$WO_3 \cdot 0.46H_2O$ had reached saturation after visible light irradiation for about 80 min. Moreover, the illuminated h-$WO_3 \cdot 0.46H_2O$ exhibited a surprising stability in air, with the absorbance of the sample LP-80 min at 700 nm decreasing by only 12% after more than 24 h (Fig. S5†), reflecting the excellent stability of the stored photogenerated electrons. The stored electrons in illuminated h-$WO_3 \cdot 0.46H_2O$ were quantified by the

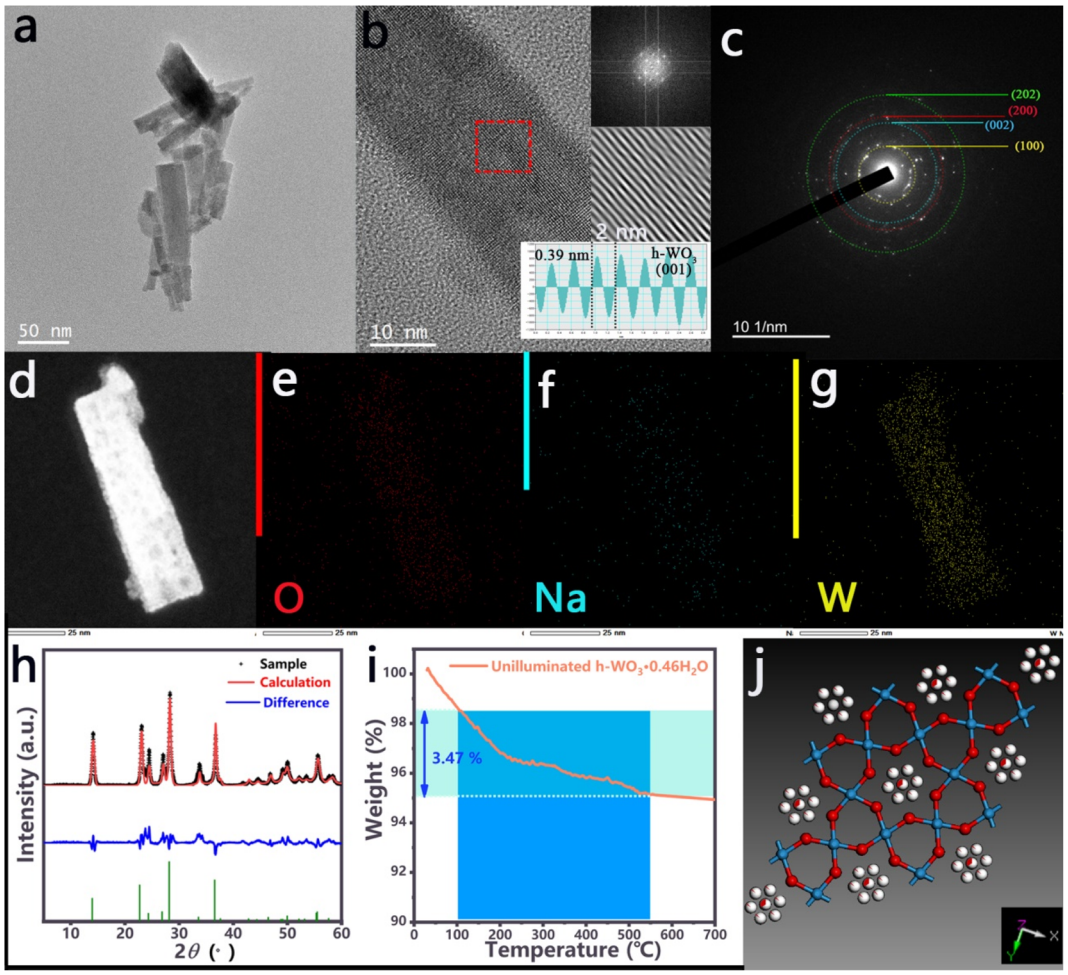

Fig. 1 (a) TEM image and (b) HR-TEM image (the inset shows the corresponding fast Fourier transform (FFT) patterns and the lattice plane intensity profile). (c) SAED patterns of h-$WO_3 \cdot 0.46H_2O$. (d) The annular dark field (ADF) image and (e–g) elemental mapping images of h-$WO_3 \cdot 0.46H_2O$. (h) XRD pattern and the Rietveld refinement of h-$WO_3 \cdot 0.46H_2O$. (i) TG curve of unilluminated h-$WO_3 \cdot 0.46H_2O$. (j) The refined crystal structure unit of h-$WO_3 \cdot 0.46H_2O$ viewed toward the xy plane.

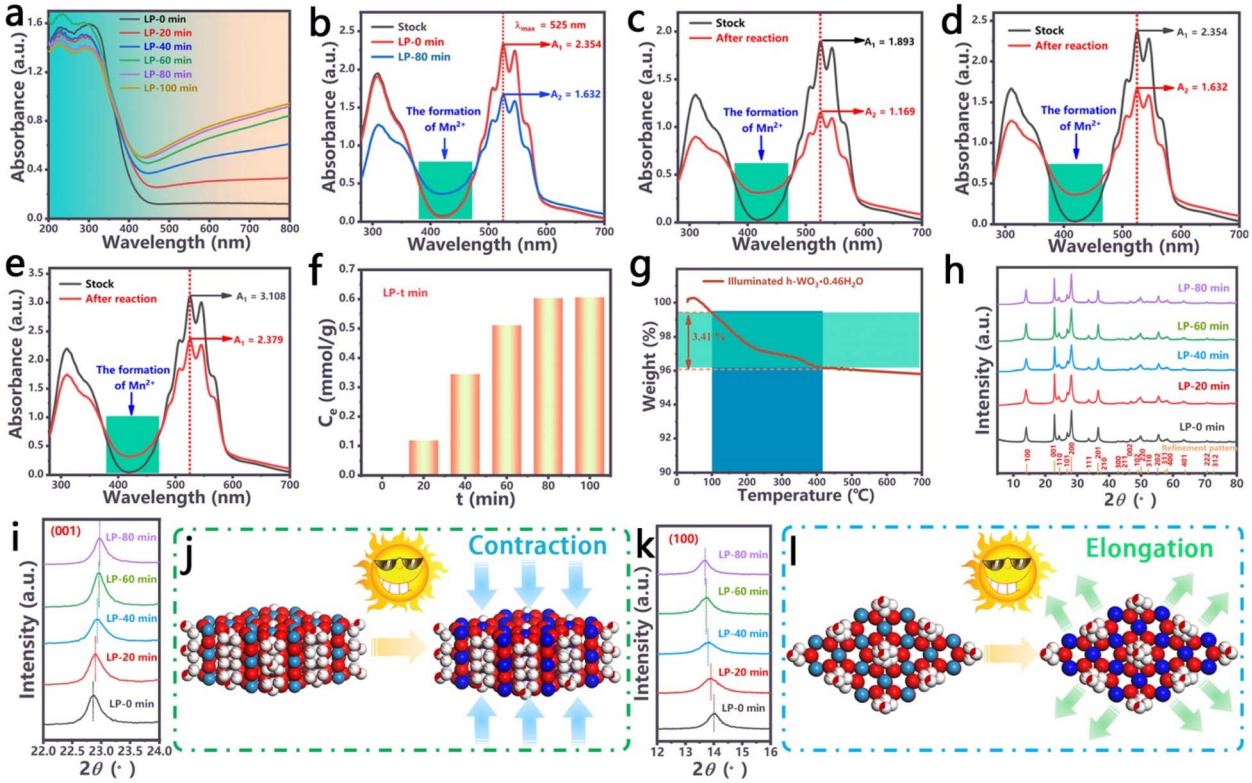

Fig. 2 (a) Absorbance spectra of different illuminated h-$WO_3 \cdot 0.46H_2O$ samples. (b) The reduction experiments of $KMnO_4$ using different catalysts. The reduction experiments of $KMnO_4$ with initial concentrations of (c) 120 ppm, (d) 150 ppm, and (e) 200 ppm using the LP-80 min catalyst. (f) The concentration of stored electrons for different illuminated h-$WO_3 \cdot 0.46H_2O$ samples. (g) TG curve of unilluminated h-$WO_3 \cdot 0.46H_2O$. (h) The XRD spectra and (i and k) partial enlarged view of XRD patterns for different illuminated h-$WO_3 \cdot 0.46H_2O$. (j and l) Schematic diagram of lattice changes for h-$WO_3 \cdot 0.46H_2O$ under illumination.

reduction experiments of $KMnO_4$ (the experimental details are displayed in Text S1.1†), in view of the good linearity between $KMnO_4$ solution concentration and absorbance (Fig. S6†). Based on the Lambert–Beer Law and the stoichiometric relationships of chemical reaction ($MnO_4^- + 5W(V) + 8H^+ - Mn^{2+} + 5W(VI) + 4H_2O$, Fig. S7†), the concentration of stored electrons for LP-80 min can be calculated to be 0.6033 mmol g^{-1} by comparing the absorbance changes of $KMnO_4$ solution before and after the reduction reaction (Fig. 2b). The reliability of the result was also validated by the reduction experiments of $KMnO_4$ solution with different initial concentrations (Fig. 2c–e). Similarly, the concentration of stored electrons for different LP-*t* min can also be obtained (Fig. 2f). Obviously, when illuminated for more than 80 min, the storage capacity of h-$WO_3 \cdot 0.46H_2O$ for photogenerated electrons is close to saturation. The above results revealed the slow rate of coloration of h-$WO_3 \cdot 0.46H_2O$ and the anomalous stability of the illuminated h-$WO_3 \cdot 0.46H_2O$, which also imply that the photochromic mechanism of h-WO_3 has its own peculiarities.

TGA of illuminated h-$WO_3 \cdot 0.46H_2O$ and XRD measurements of h-$WO_3 \cdot 0.46H_2O$ with different illumination times were performed to investigate the mass change and phase evolution of the sample during the photochromic process. As shown in Fig. 2g, the mass attenuation in the range of >100 °C was 3.41%, which is very close to that of the unilluminated h-$WO_3 \cdot 0.46H_2O$, reflecting that no significant loss of lattice water of h-$WO_3 \cdot 0.46H_2O$ occurred before and after illumination. In addition, the XRD diffraction peaks of h-$WO_3 \cdot 0.46H_2O$ were well preserved after illumination (Fig. 2h), indicating that irradiation only changed its color but did not affect its crystal phase. However, changes in the position of the diffraction peaks can still be observed from the partial magnified view of the XRD patterns. During illumination, the (0 0 1) diffraction peak of h-$WO_3 \cdot 0.46H_2O$ gradually shifted to the high angle direction with the increase of time (Fig. 2i), reflecting the structural contraction of the crystal lattice along the *z* axis that occurred in h-$WO_3 \cdot 0.46H_2O$ (Fig. 2j), which may be caused by the strong interaction between the protons originating from the lattice water and the bridging oxygen atoms during the formation of H_xWO_3. Also, the (1 0 0) peak shifts to the left (Fig. 2k), suggesting the elongation of the crystal along the *xy* plane (Fig. 2l), which also indicates the existence of such strong interaction. The lattice elongation along the *xy* plane and crystal contraction along the *z* axis facilitate the entry of water molecules into the lattice of h-$WO_3 \cdot 0.46H_2O$ from outside to replenish the lattice water molecules consumed by the photochromic effect.

To further clarify the particular photochromic mechanism of h-$WO_3 \cdot 0.46H_2O$, additional spectroscopic tests were used to analyse the surface electronic state and chemical structure of h-$WO_3 \cdot 0.46H_2O$ before and after light irradiation. Full XPS

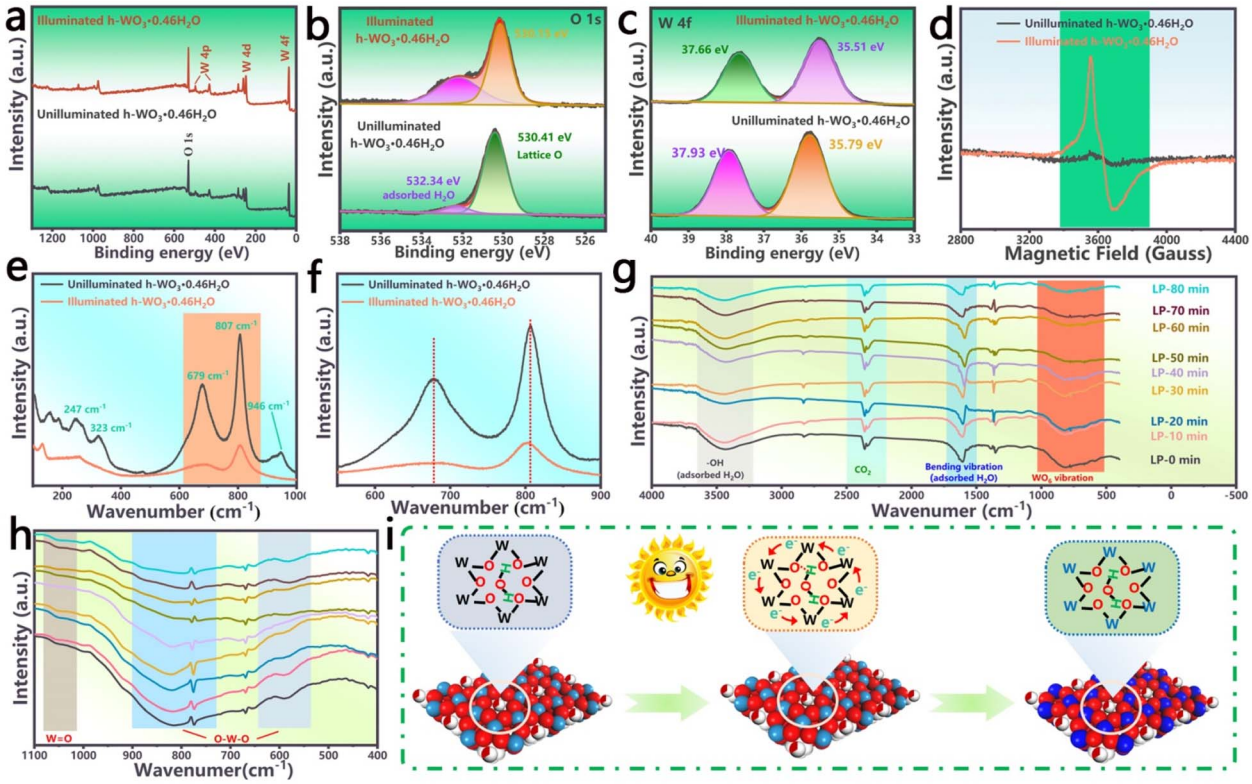

Fig. 3 (a) XPS survey spectra of h-$WO_3 \cdot 0.46H_2O$ before and after illumination. High resolution XPS spectra of (b) O 1s and (c) W 4f in unilluminated h-$WO_3 \cdot 0.46H_2O$ and illuminated h-$WO_3 \cdot 0.46H_2O$. (d) The EPR profiles and (e) Raman spectra of h-$WO_3 \cdot 0.46H_2O$ before and after illumination. (f) The partial enlarged view of Raman patterns of the samples. (g) The FT-IR spectra and (h) partial enlarged view of FT-IR spectra for h-$WO_3 \cdot 0.46H_2O$ with different illumination times. (i) Schematic illustration of photochromism process for h-$WO_3 \cdot 0.46H_2O$.

spectra (Fig. 3a) showed that W and O are the major elements in the samples without other impurity elements. In addition, the high resolution XPS model was performed to study the chemical state of O and W elements. After convolution of the XPS spectra, both O 1s and W 4f spectra exhibit two individual peaks. The peaks at 530.49 eV and 532.34 eV in the O 1s spectrum of the unilluminated h-$WO_3 \cdot 0.46H_2O$ are assigned to the lattice O in hexagonal WO_3 and the adsorbed water molecules on the surface of the sample (Fig. 3b),[24–27] respectively. As for the W 4f spectrum of the unilluminated h-$WO_3 \cdot 0.46H_2O$, the two peaks at 35.79 eV and 37.93 eV are attributed to the spin–orbit splitting of the W 4f components (W $4f_{7/2}$ and W $4f_{5/2}$) (Fig. 3c).[28–30] After visible light irradiation, both the O 1s and W 4f peaks of h-$WO_3 \cdot 0.46H_2O$ shifted toward the lower binding energy, indicating that the photochromic process of h-$WO_3 \cdot 0.46H_2O$ was accompanied by an increase in the local electron density of O and W.[31] The electron paramagnetic resonance (EPR) spectra (Fig. 3d) of the illuminated h-$WO_3 \cdot 0.46H_2O$ showed a sharp signal at about 3600 G with $g = 1.792$ compared to the unilluminated h-$WO_3 \cdot 0.46H_2O$, reflecting the existence of W^{5+},[32,33] which can be attributed to the increase in the electron cloud density of W due to the excitation of visible light and coincides with the XPS results.

Raman and FT-IR spectra provide detailed information on the surface functional groups and chemical bonds of the samples to analyze the changes of h-$WO_3 \cdot 0.46H_2O$ before and after light illumination. From the results of Raman measurements, the peaks assigned to the W–O–W bending modes/the bending vibration δ (W^{6+}–O) (247 cm^{-1}, 323 cm^{-1}),[34] O–W–O stretching modes (679 cm^{-1}, 807 cm^{-1})[34–36] and the stretching vibration of terminal W=O bonds (946 cm^{-1})[34,35] of h-$WO_3 \cdot 0.46H_2O$ were substantially attenuated after illumination (Fig. 3e), suggesting that the chemical bond between W and O in h-$WO_3 \cdot 0.46H_2O$ was seriously weakened by the strong interaction between the protons originating from lattice water and the bridging oxygen atoms. In addition, the partial enlarged view of Raman patterns of the samples (Fig. 3f) showed that the dominant peaks of illuminated h-$WO_3 \cdot 0.46H_2O$ shifted toward the lower wavenumber compared to the unilluminated sample, also verifying the change in Raman vibrational energy level due to the interaction between the protons from lattice water and the bridging oxygen atoms. As shown in Fig. 3g, all the samples exhibited similar IR absorption spectra including the main IR absorption peaks at 3430 cm^{-1} (the stretching vibrations of surface absorbed water),[31,35] 2380 cm^{-1} (asymmetric stretching vibrations of surface absorbed CO_2),[37] 1610 cm^{-1} (the bending vibrations of surface absorbed water)[31,38] and 1100–500 cm^{-1} (the typical WO_6 vibration bands include the O–W–O band and W=O band).[34,35] Noteworthily, the bending vibration peak of surface absorbed water for illuminated h-$WO_3 \cdot 0.46H_2O$ showed an obvious red shift compared to unilluminated h-$WO_3 \cdot 0.46H_2O$, which can be ascribed to the compensation

effect of external water molecules on lattice water molecules. Additionally, the vibrational absorption of O–W–O and W=O for h-$WO_3 \cdot 0.46H_2O$ decreased gradually with increasing irradiation time (Fig. 3h). The results are consistent with the results of XRD and Raman measurements.

From the results of the above series of spectroscopic tests, the stable photochromic process of h-$WO_3 \cdot 0.46H_2O$ can be reasonably explained (the schematic illustration is shown in Fig. 3i): under visible light irradiation, the local electronic density of h-$WO_3 \cdot 0.46H_2O$ increases and lattice water located in the dodecagon tunnels along the *z*-axis of h-WO_3 is decomposed. The generated protons then interact with the bridging oxygen atoms in the WO_6 structure, leading to the weakening of O–W–O as well as W=O bonds. Meanwhile, the interaction also induces a distortion of the h-$WO_3 \cdot 0.46H_2O$ lattice (lattice relaxation along the *xy* plane and contraction along the *z* axis), which helps the external water molecules to replenish the lattice water molecules consumed by the photochromic effect. It is due to this special photochromic mechanism that the illuminated h-$WO_3 \cdot 0.46H_2O$ can maintain its color stability in air for a long time.

In our study, the blue color of the illuminated h-$WO_3 \cdot 0.46H_2O$ does not easily fade in air, it can be decolorized by the oxidation of strong oxidizing agents (*e.g.*, H_2O_2), and the oxidation experiments of I^- (the experimental details are shown in Text S1.2†) were carried out to monitor the consumption of H_2O_2. As shown in Fig. 4a, the absorbance of I_3^- is very close only in the H_2O_2 and unilluminated h-$WO_3 \cdot 0.46H_2O/H_2O_2$ systems, indicating that the unirradiated h-$WO_3 \cdot 0.46H_2O$ did not react significantly with H_2O_2. As for the illuminated h-$WO_3 \cdot 0.46H_2O$ sample, its blue colour gradually fades after the addition of H_2O_2 (inset in Fig. 4a), reflecting the gradual conversion of the W(v) species formed through light illumination to W(vi) species. Interestingly, the characteristic absorbance of I_3^- in illuminated h-$WO_3 \cdot 0.46H_2O/H_2O_2$ did not decrease but exhibited a significant increase compared to that in the H_2O_2 or unilluminated h-$WO_3 \cdot 0.46H_2O/H_2O_2$ systems. Besides, Fig. 4b showed that illuminated h-$WO_3 \cdot 0.46H_2O$ has a considerably greater H_2O_2 reduction current in the dark compared to unilluminated h-$WO_3 \cdot 0.46H_2O$, and the H_2O_2 reduction current on illuminated h-$WO_3 \cdot 0.46H_2O$ increased with increasing the addition amount of 10 wt% H_2O_2 solution from 30 to 150 μL (Fig. 4c). This proves that there is a unique electron transfer between illuminated h-$WO_3 \cdot 0.46H_2O$ and H_2O_2 from the former to the latter. The above surprising results

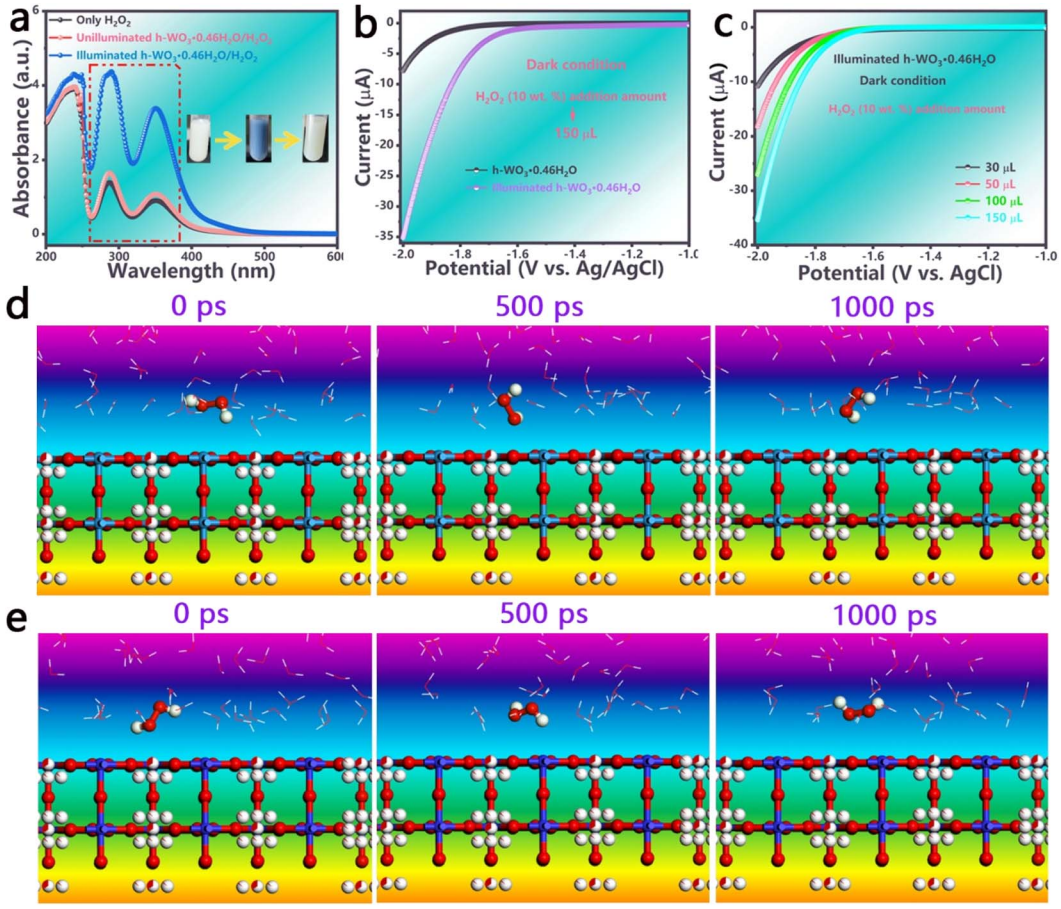

Fig. 4 (a) The oxidation experiments of I^- for different catalysts. (b) LSV curves of the electrode of unilluminated h-$WO_3 \cdot 0.46H_2O$ and illuminated h-$WO_3 \cdot 0.46H_2O$ in the presence of 150 μL H_2O_2 (10 wt%) in 30 ml N_2-saturated 0.5 M $NaNO_3$ solution under dark conditions. (c) LSV curves of the illuminated h-$WO_3 \cdot 0.46H_2O$ electrode in 30 ml N_2-saturated 0.5 M $NaNO_3$ solution containing different [H_2O_2] under dark conditions. MD simulation for (d) unilluminated h-$WO_3 \cdot 0.46H_2O/H_2O_2$ and (e) illuminated h-$WO_3 \cdot 0.46H_2O/H_2O_2$ systems.

suggest that the illuminated h-$WO_3 \cdot 0.46H_2O$ does not undergo the expected oxidation process in the presence of H_2O_2, but rather exhibits the activity of Fenton reaction, resulting in more efficient oxidation of I^- by generating more reactive oxygen species (ROS).

To further comprehend the process underlying the activation of H_2O_2 molecules by the illuminated h-$WO_3 \cdot 0.46H_2O$, the H_2O_2 adsorption on the (001) surface of the h-$WO_3 \cdot 0.46H_2O$ before and after illumination was compared by theoretical calculations (Text S1.3†). From the molecular dynamics (MD) simulations, the H_2O_2 molecule with one side protruding toward the vacuum binds to the (001) surface of unilluminated h-$WO_3 \cdot 0.46H_2O$ (Fig. 4d), which is clearly not conducive to adequate contact between the O–O bond and the catalyst surface. Contrarily, the H_2O_2 molecule can be permanently adsorbed horizontally on the (001) surface of illuminated h-$WO_3 \cdot 0.46H_2O$ (Fig. 4e). The favorable contact between the H_2O_2 molecule and illuminated h-$WO_3 \cdot 0.46H_2O$ (001) surface creates the conditions for the activation step of the O–O bond.

In addition, the H_2O_2 adsorption on the (001) surface of the h-$WO_3 \cdot 0.46H_2O$ before and after illumination was also analysed from a thermodynamic perspective. As presented in Fig. 5a, the E_a of H_2O_2 for illuminated h-$WO_3 \cdot 0.46H_2O$ is −2.89 eV, much more negative than that of the unilluminated sample (−1.57 eV), which means that the H_2O_2 molecule is more easily adsorbed on the surface of illuminated h-$WO_3 \cdot 0.46H_2O$ than unilluminated h-$WO_3 \cdot 0.46H_2O$.[39] Moreover, the longer length (3.145 Å, Fig. 5b) of O–O bond of H_2O_2 molecule adsorbed on illuminated h-

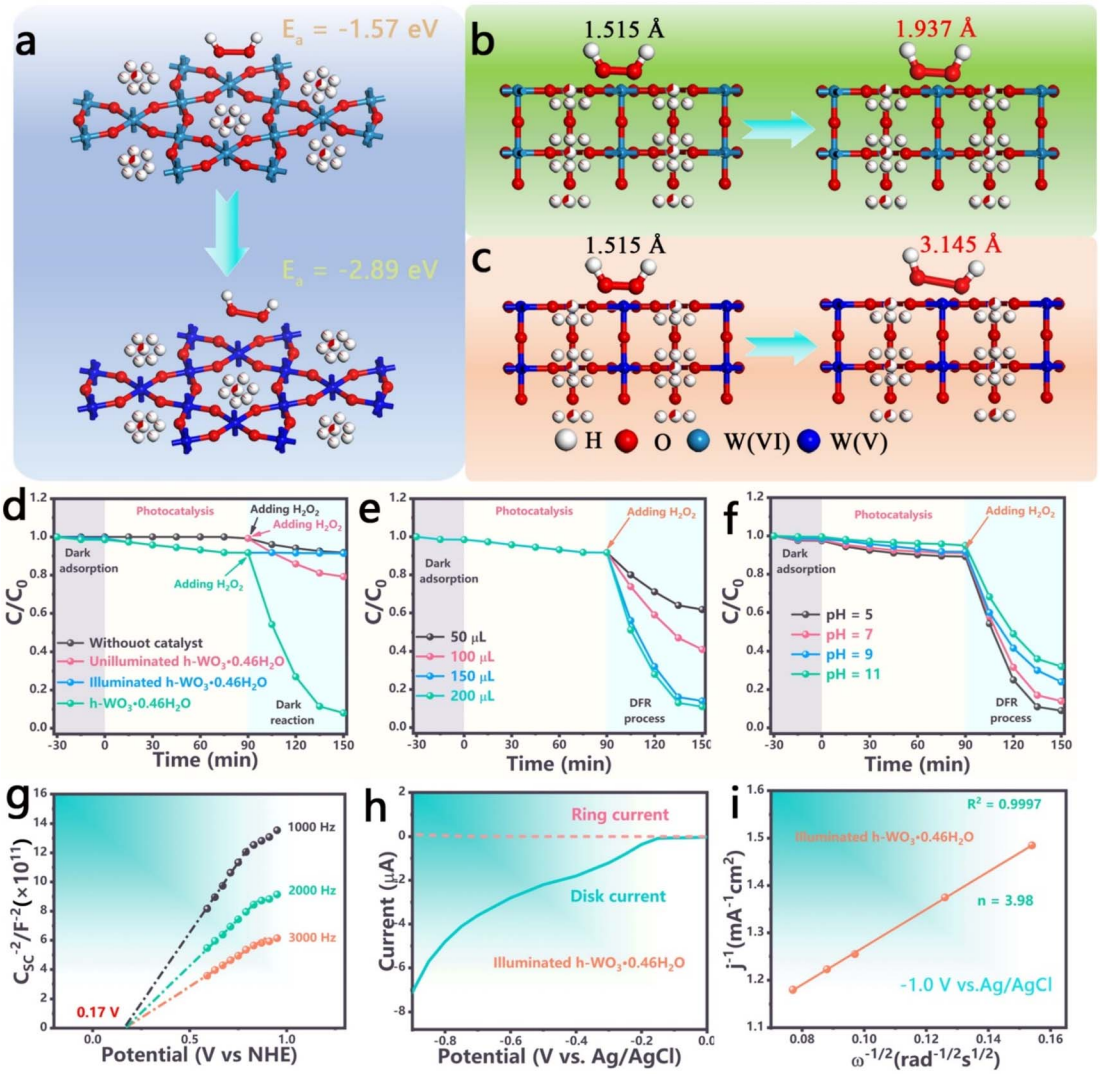

Fig. 5 (a) E_a (adsorption energy) of H_2O_2 on the (0 0 1) surfaces of unilluminated and illuminated h-$WO_3 \cdot 0.46H_2O$. The variations in O–O bond length of the H_2O_2 molecule before and after its adsorption on the (0 0 1) surface of (b) unilluminated and (c) illuminated h-$WO_3 \cdot 0.46H_2O$. (d) The comparison of concentration of DNBP degradation in h-$WO_3 \cdot 0.46H_2O$ under different conditions. Degradation of DNBP with illuminated h-$WO_3 \cdot 0.46H_2O$ *via* the DFR process under different (e) amounts of H_2O_2 solution (10 wt%) and (f) pH values. (g) Mott–Schottky plots at different testing frequencies for unilluminated h-$WO_3 \cdot 0.46H_2O$. (h) RRDE polarization curves over the illuminated h-$WO_3 \cdot 0.46H_2O$ electrode at 1600 rpm in O_2-saturated electrolyte using the ring current and the disk current. (i) Koutecky–Levich (K–L) plots obtained *via* RDE analysis in an O_2-saturated solution at −1.0 V (*vs.* Ag/AgCl) under the dark condition.

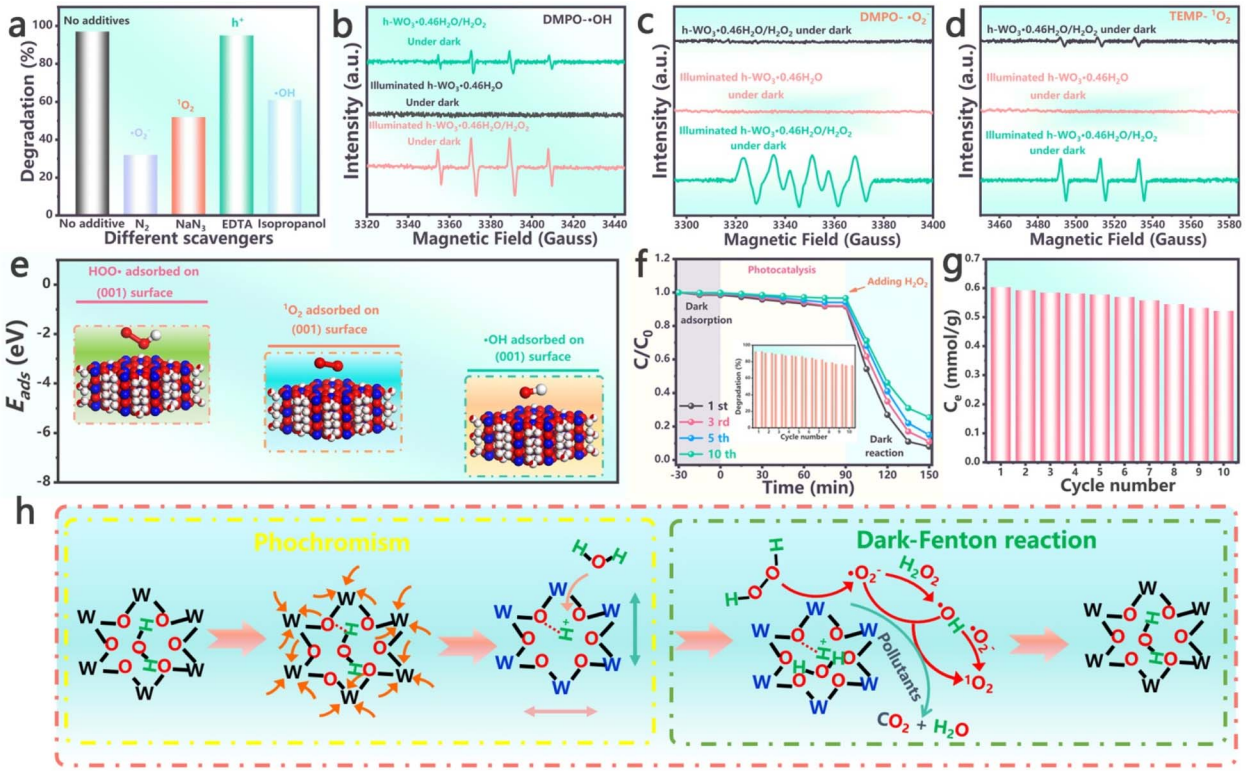

Fig. 6 (a) Trapping experiments of reactive species with illuminated h-$WO_3 \cdot 0.46H_2O/H_2O_2$ in the dark. (b–d) EPR signals of $^{\bullet}OH$, $^{\bullet}O_2^-$, and $^1O_2$ in the presence of DMPO, DMPO, and TEMP among different reaction systems, respectively. (e) The adsorption energy diagrams for $HOO^{\bullet}$, $^1O_2$ and $^{\bullet}OH$ on the (0 0 1) surface of illuminated h-$WO_3 \cdot 0.46H_2O$. (f) The reusability of h-$WO_3 \cdot 0.46H_2O$ for degradation of DNBP *via* dark adsorption-photodegradation-DFR process. (g) The concentration of stored electrons for LP-80 min through different cycle times. (h) Schematic illustration of the photochromic mechanism and DFR mechanism for h-$WO_3 \cdot 0.46H_2O$.

$WO_3 \cdot 0.46H_2O$ compared with unilluminated h-$WO_3 \cdot 0.46H_2O$ (1.937 Å, Fig. 5c) indicates the activation tendency. Adequate contact between the H_2O_2 molecule and illuminated h-$WO_3 \cdot 0.46H_2O$ (001) surface can facilitate the activation of the O–O bond. Based on the above results of theoretical calculations, it can be easily drawn that the enhanced thermodynamic and kinetic ability of h-$WO_3 \cdot 0.46H_2O$ to adsorb H_2O_2 molecules after illumination creates the conditions for the initiation of the ensuing Fenton reaction.

DNBP was employed as the target pollutant to better illustrate the dark-Fenton reaction (DFR) activity of illuminated h-$WO_3 \cdot 0.46H_2O$ (Fig. 5d and Text S2.6†). Under illumination, the DNBP degradation performance of h-$WO_3 \cdot 0.46H_2O$ was so weak and just ~7% of DNBP was removed in 2 h. After turning off the light, the concentration of DNBP in illuminated h-$WO_3 \cdot 0.46H_2O$ remained almost constant, which indicated that the stored electrons in illuminated h-$WO_3 \cdot 0.46H_2O$ cannot induce the degradation of the target pollutant. However, more than 80% of DNBP in illuminated h-$WO_3 \cdot 0.46H_2O$ was removed in 1 h after adding H_2O_2, which far exceeded the activity of only H_2O_2 (11%) and unilluminated h-$WO_3 \cdot 0.46H_2O/H_2O_2$ (24%) under the same conditions, reflecting the activation of H_2O_2 by illuminated h-$WO_3 \cdot 0.46H_2O$. Furthermore, optimization of reaction conditions (Fig. 5e and f) and TOC removal amount (Fig. S8†) were explored. To further clarify the role of the stored electrons in illuminated h-$WO_3 \cdot 0.46H_2O$, a series of electrochemical tests were carried out. As shown in Fig. 5g, the Mott–Schottky curve at different testing frequencies exhibited a positive slope (n-type characteristic[40,41]) and a flat band potential of 0.17 V *vs.* NHE; therefore, the conduction band edge (E_{CB}) of h-$WO_3 \cdot 0.46H_2O$ is 0.17 V *vs.* NHE.[42,43] Owing to the positive E_{CB}, illuminated h-$WO_3 \cdot 0.46H_2O$ cannot reduce O_2 by the single-electron pathway (eqn (3)). Besides that, the reduction disk current (I_D) and the oxidation ring current (I_R) under different potential of the illuminated h-$WO_3 \cdot 0.46H_2O$ electrode in O_2-saturated solution are shown in Fig. 5h. The invisible I_R and distinct I_D can be observed since the storage electrons in illuminated h-$WO_3 \cdot 0.46H_2O$ were constantly consumed by the O_2 molecule, and the average electron transfer number on illuminated h-$WO_3 \cdot 0.46H_2O$ can be estimated to be ~4 by the formula (Text 2.7). The linear regression result of the Koutecky–Levich (K–L) plot showed that the number of electron transfer involved in the overall O_2 reduction was 3.98 (Fig. 5i and Text 2.7), which was in good agreement with the RRDE result. So, the illuminated h-$WO_3 \cdot 0.46H_2O$ in aqueous solution in the dark induces the four-electron ORR pathway (eqn (7)) to produce H_2O rather than the single-electron (eqn (3)) or two-electron pathway (eqn (6)) to generate H_2O_2, which thermodynamically demonstrates that the stored electrons in illuminated h-$WO_3 \cdot 0.46H_2O$ cannot generate ROS *via* the ORR pathway in the dark.

The type of active species is important for understanding the mechanism of the DFR process; trapping experiments of reactive species among different systems in the dark are carried out to explore the contribution of different active species. Fig. 6a displayed that the degradation of DNBP was obviously suppressed after introducing high purity nitrogen or NaN_3 or isopropanol, indicating that $^{\bullet}O_2^-$, $^1O_2$ and $^{\bullet}OH$ were the active species in the process of DNBP degradation with the illuminated h-$WO_3 \cdot 0.46H_2O/H_2O_2$ system in the dark. It can be also observed from the figure that the $^{\bullet}O_2^-$ is the prominent active species in the DFR process and the role of $^1O_2$ is also important. Furthermore, EPR measurements can also clearly show the kind of reactive species produced during the process of Fenton reaction. As shown in Fig. 6b, the illuminated h-$WO_3 \cdot 0.46H_2O/H_2O_2$ system exhibits the apparently stronger signal of $^{\bullet}OH$ than the unilluminated h-$WO_3 \cdot 0.46H_2O/H_2O_2$ system and illuminated h-$WO_3 \cdot 0.46H_2O$, which not only indicates that the electrons stored in illuminated h-$WO_3 \cdot 0.46H_2O$ cannot contribute to the degradation of the target pollutant directly, but also demonstrates its excellent activation capacity of H_2O_2. Similar results can be seen from the EPR spectra of DMPO-$^{\bullet}O_2^-$ and TEMP-$^1O_2$ (Fig. 6c and d).

To better understand the process by which reactive species are produced on the catalyst surface, the adsorption energy of $HOO^{\bullet}$ (since $^{\bullet}O_2^-$ is a Brønsted base with pK_a = 9.12,[44,45] the protonated form is used in the process of theoretical calculation), $^1O_2$ and $^{\bullet}OH$ on the illuminated h-$WO_3 \cdot 0.46H_2O$ (0 0 1) surface was calculated by the DFT method, respectively. As shown in Fig. 6e, the values of E_{ads} for $HOO^{\bullet}$, $^1O_2$ and $^{\bullet}OH$ are −0.70 eV, −2.49 eV and −3.48 eV, respectively. The smaller value of E_{ads} indicates that the adsorption between the adsorbent and adsorbate is unstable and adsorbate molecules are easily desorbed from the surface of the adsorbent.[46] Apparently, $HOO^{\bullet}$ is more likely than $^1O_2$ and $^{\bullet}OH$ to leave the surface of illuminated h-$WO_3 \cdot 0.46H_2O$ and participate in the degradation reaction of DNBP. In addition, if the dominant active species directly produced by the illuminated h-$WO_3 \cdot 0.46H_2O/H_2O_2$ system is $^1O_2$ or $^{\bullet}OH$, these two ROS will oxidize W(v) to W(vi) because they are difficult to desorb from the surface of illuminated h-$WO_3 \cdot 0.46H_2O$, which will cause the activity of the catalyst to decay and is inconsistent with experimental results. It can be concluded that the directly active species for the activation of H_2O_2 with illuminated h-$WO_3 \cdot 0.46H_2O$ is $^{\bullet}O_2^-$, and the formation of $^1O_2$ and $^{\bullet}OH$ is most likely the result of a chain reaction caused by $^{\bullet}O_2^-$. In light of this, the generation of $^{\bullet}O_2^-$, $^{\bullet}OH$ and $^1O_2$ in the illuminated h-$WO_3 \cdot 0.46H_2O/H_2O_2$ system in the dark can be demonstrated by the routes below (eqn (12)–(16)):[47–50]

$$[W_VO_6] + H_2O_2 \rightleftharpoons [O_6W_V(O_2H_2)] \quad (12)$$

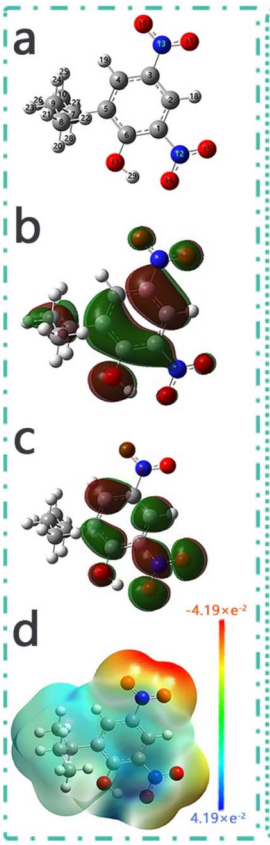

e

Atom	Fukui (0)		Fukui (-)		Fukui (+)	
	Mulliken	Hirshfeld	Mulliken	Hirshfeld	Mulliken	Hirshfeld
C (1)	0.048	0.061	0.023	0.043	0.074	0.078
C (2)	0.047	0.051	0.020	0.023	0.074	0.079
C (3)	0.012	0.041	0.023	0.046	0.001	0.035
C (4)	0.070	0.076	0.047	0.058	0.093	0.094
C (5)	0.050	0.053	0.019	0.033	0.061	0.072
C (6)	0.043	0.049	0.065	0.067	0.022	0.031
C (7)	0.073	0.078	0.069	0.072	-0.028	0.006
C (8)	-0.014	0.009	-0.013	0.007	-0.016	0.011
C (9)	-0.014	0.007	-0.013	0.005	-0.016	0.008
C (10)	-0.009	0.004	-0.007	0.004	-0.011	0.005
O (11)	0.047	0.052	0.069	0.075	0.025	0.030
N (12)	0.056	0.061	0.079	0.083	0.033	0.039
N (13)	0.052	0.065	0.063	0.071	0.021	0.019
O (14)	0.049	0.049	0.052	0.051	0.046	0.046
O (15)	0.041	0.058	0.047	0.053	0.035	0.063
O (16)	0.053	0.060	0.058	0.065	0.028	0.035
O (17)	0.035	0.041	0.059	0.066	0.030	0.036

Fig. 7 (a) The optimized molecular structure, (b) HOMO (−0.269 eV), (c) LUMO (−0.118 eV), and (d) electrostatic surface potential (ESP) of DNBP. (e) Fukui indices (e Å^{-3}) of the DNBP molecule.

$$[O_6W_V(O_2H_2)] + H_2O_2 \rightarrow [W_{VI}O_6] + {}^{\cdot}O_2^- + 2H_2O \quad (13)$$

$${}^{\cdot}O_2^- + H_2O_2 \rightarrow {}^{\cdot}OH + O_2 + OH^-, \text{ Haber–Weiss reaction}, \Delta G = -0.64 \text{ eV} = -62 \text{ kJ mol}^{-1} \quad (14)$$

$$2{}^{\cdot}O_2^- + 2H_2O \rightarrow {}^1O_2 + H_2O_2 + 2OH^-, \Delta G = -0.65 \text{ eV} = -63.3 \text{ kJ mol}^{-1} \quad (15)$$

$${}^{\cdot}O_2^- + {}^{\cdot}OH \rightarrow {}^1O_2 + OH^-, \Delta G = -1.31 \text{ eV} = -127 \text{ kJ mol}^{-1} \quad (16)$$

The reusability and stability of the catalyst were evaluated by 10 cycles of experiment. After 10 cycles, the DNBP degradation efficiency decreased from 92.3% to 75.6% (Fig. 6f), accompanied by the TOC removal also decreasing from 82.1% to 62.6% (Fig. S9a†), which can be ascribed to the reduction in the number of ROS generated from the DFR process with increasing cycle number (Fig. S9b†). Additionally, the capacity of stored electrons also reduced from 0.6033 mmol g^{-1} to 0.5218 mmol g^{-1}. The above results suggested that 80% of the performance of h-$WO_3 \cdot 0.46H_2O$ was retained after 10 cycles, reflecting the good recyclability of the catalyst. Furthermore, the cycle experiments had no discernible effects on the crystal phase of h-$WO_3 \cdot 0.46H_2O$ (Fig. S10†). The tremendous potential of h-$WO_3 \cdot 0.46H_2O$ in practical applications is indicated by its exceptional performance and structure stability.

After the analysis and discussion mentioned above, the reasonable cycle mechanism for h-$WO_3 \cdot 0.46H_2O$ under all-weather conditions is proposed in Fig. 6h. Under the excitation of visible or solar light, the electron storage effect initiated by the process of W(VI) → W(V) increases the local electronic

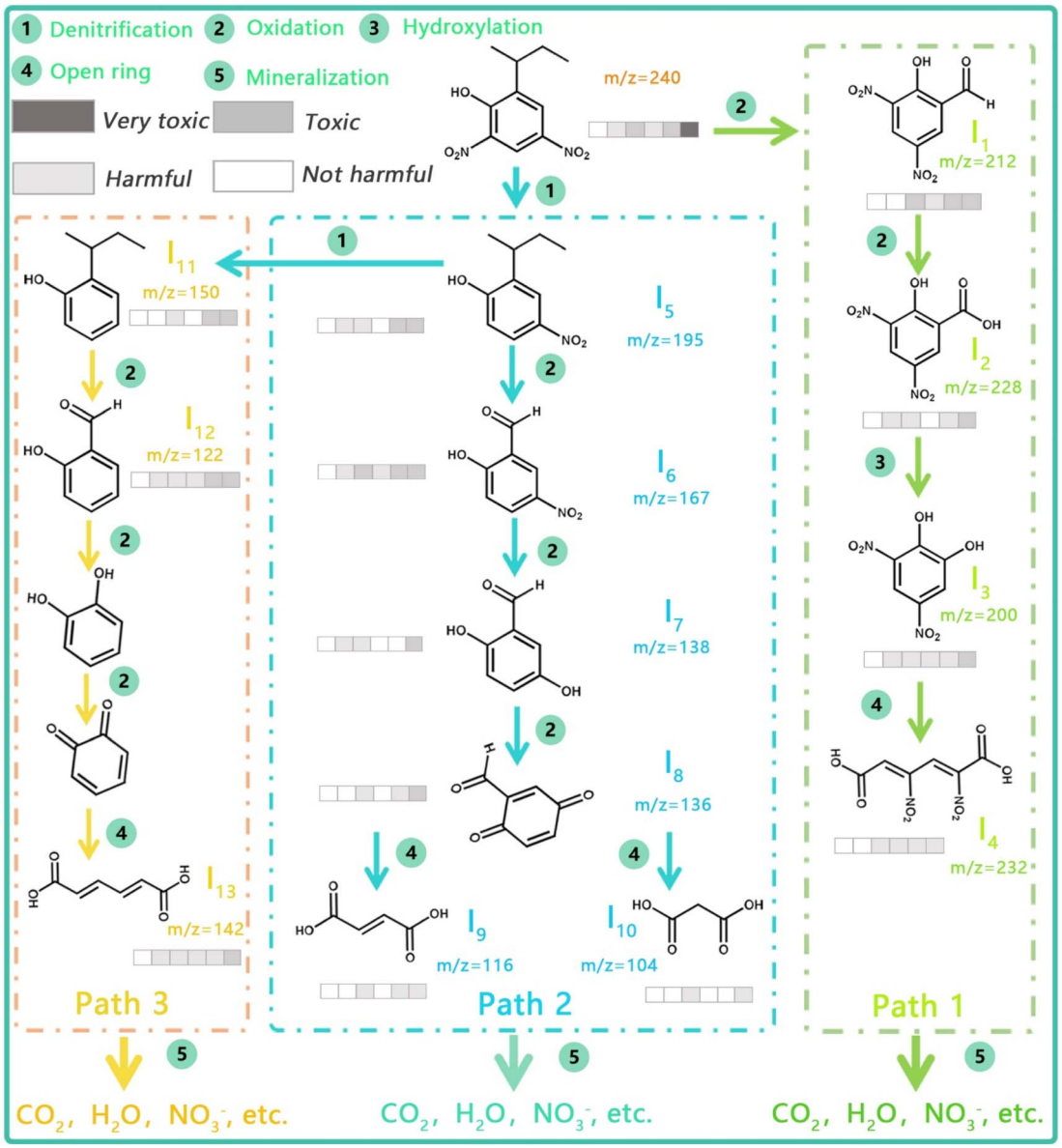

Fig. 8 The degradation pathway of DNBP in the illuminated h-$WO_3 \cdot 0.46H_2O/H_2O_2$ system in the dark and the toxicity evolution of intermediates in the degradation pathways estimated *via* ECOSAR.

density of h-$WO_3 \cdot 0.46H_2O$ and the protons originating from lattice water located in the dodecagon tunnels along the *z* axis interact with the nearby bridging oxygen atoms in the lattice, which causes the colour of h-$WO_3 \cdot 0.46H_2O$ to change from white to blue and the distortion of its lattice in the horizontal and vertical directions, respectively. The lattice change also promotes the entry of water molecules from outside into the lattice of h-$WO_3 \cdot 0.46H_2O$ to replenish the lattice water molecules consumed by the photochromic effect. In the dark, the exogenous H_2O_2 molecule tends to adsorb horizontally on the surface of illuminated h-$WO_3 \cdot 0.46H_2O$ under thermodynamic and kinetic driving forces. Subsequently, the adsorbed H_2O_2 molecule is activated by the stored electrons in illuminated h-$WO_3 \cdot 0.46H_2O$ and $^{\bullet}O_2^-$, $^{\bullet}OH$ and $^1O_2$ are efficiently produced. Accordingly, it is possible to see the excellent DFR activity of illuminated h-$WO_3 \cdot 0.46H_2O$. In the bargain, the altered colour and structure of h-$WO_3 \cdot 0.46H_2O$ due to illumination is also restored by the depletion of the stored electrons.

The transformation of the structure of organic pollutant molecules during degradation is closely related to the reactivity of its different moieties. As shown in Fig. 7a, the DNBP molecule was constructed and optimized by GaussView before calculation (the details of the calculation are shown in Text S1.3†). After that, a series of theoretical calculations based on density functional theory (DFT) were carried out to investigate the reactivity of different regions of the DNBP molecule. The C (1–6), N (12), O (11), O (14) and O (15) atoms in the DNBP molecule have the majority of the HOMO and LUMO orbitals (Fig. 7b and c), demonstrating that these atoms are more susceptible to assault.[51–53] In addition, the electrostatic surface potential (ESP) distribution diagram (Fig. 7d) of DNBP intuitively showed the location with red color of negatively charged centers in the molecule.[54] The two nitro groups are directly attached to the benzene ring and have a higher surface electron cloud density, thus making them susceptible to attack by species with strong oxidizing capacity.[55,56] According to the Fukui indices of the DNBP molecule shown in Fig. 7e, the C (1), C (2), C (4–7), N (12 and 13), O (14) and O (16) atoms have a high Fukui (0) index, which indicate that these sites have the theoretically higher radical reactivity.[57–59] The C (4), C (6, 7), N (12 and 13) and O (11, 14–17) have considerable electrophilic reactivity as indicated by their Fukui (−) indexes.[58–61]

The genuine degradation paths of DNBP molecules in the illuminated h-$WO_3 \cdot 0.46H_2O/H_2O_2$ system are obtained by GC-MS tests in addition to DFT calculations. Based on a rigorous analysis of the MS spectra (Fig. S11 and Table S3†) of the reaction intermediates, two main rational pathways are proposed (Fig. 8). As displayed in Fig. 8, N (12) is assaulted firstly by the ROS and the o-nitro group leaves. Then, the obtained 2-*sec*-4-nitro-butylphenol intermediate undergoes two routes of degradation reactions simultaneously. On the one hand, the N (13) site is next attacked to cause the departure of the p-nitro group (path 1), and the formed intermediate is immediately followed by a series of oxidation reactions (the reaction sites are C (5–7)) and is finally mineralized; on the other hand, the C (7) atom as the reactive site is oxidized (path 2) and then continuous oxidation and ring opening with N (13) and C (1–4, 6) atoms as the reaction centers occur one after another. The pathway 3 seems to be much easier than paths 1 and 2: the C (7) site is oxidized firstly by ROS and the formaldehyde group is formed. Next, the C (7) site stays as the reaction site as the intermediate formed in the previous step passes through oxidation and hydroxylation reaction. Afterwards, C (5) and C (6) as reactive sites are attacked and the ring opening reaction is induced. Finally, the product generated by ring opening reaction is mineralized. It is obvious that the reactive sites obtained from the results of DFT calculation can basically match with the above degradation pathways. In the bargain, an intuitive conclusion can also be seen in Fig. 8 that the toxicity of intermediates in the degradation process of DNBP gradually decreases with the increase of reaction time, which indicated that the removal path of DNBP by the DFR process was efficient and safe.

4 Conclusions

In conclusion, a hexagonal tungsten oxide hydrate (h-$WO_3 \cdot 0.46H_2O$) was synthesized and intensively investigated based on a series of characterizations and experiments. By the Rietveld refinement of the XRD spectra of h-$WO_3 \cdot 0.46H_2O$, the lattice water molecules can be presumed to be in the dodecagon tunnels along the *z* axis and reside between W–O layers along the *z* axis. Under visible light illumination, h-$WO_3 \cdot 0.46H_2O$ showed slow discoloration (white—blue) and the lattice water gradually decomposed. Owing to the strong interaction between the protons originating from lattice water and the bridging oxygen atoms (W–O–W), the blue colour of illuminated h-$WO_3 \cdot 0.46H_2O$ can remain stable for a long time (>24 h). More interestingly, the stored electrons due to photochromic effect in illuminated h-$WO_3 \cdot 0.46H_2O$ can effectively activate H_2O_2 and quickly degrade DNBP in the dark. On the basis of the experimental and theoretical findings, the mechanism of ROS ($^{\bullet}O_2^-$, $^{\bullet}OH$ and $^1O_2$) formation and potential pathways for DNBP degradation were eventually clarified. Our proposed mechanism, which is more reasonable and excludes the $1e^-/2e^-$ ORR pathway in the dark, is different from the more nebulous all-weather processes of WO_3-containing photocatalysts that have been reported. Our work demonstrates that the photo-storage electrons in h-$WO_3 \cdot 0.46H_2O$ activate H_2O_2 to form ROS and excludes the possibility that it generates reactive oxygen species through the mechanism previously reported in the literature, which may attract more researchers to pay attention to the reaction ability of photo-storage electrons in WO_3. In addition, we have only studied the activation effect of photo-storage electrons in h-$WO_3 \cdot 0.46H_2O$ on H_2O_2, but more valuable chemical processes may also be triggered by the photo-storage electrons, which may have more scientific questions to be explored.

Author contributions

Hao Huang: conceptualization, data curation, methodology, validation, formal analysis, riting – original draft preparation, investigation, visualization, writing – review & editing,

resources. Hui-Long Wang: conceptualization, supervision, project administration, resources, writing – review & editing, funding acquisition. Wen-Feng Jiang: writing-review & editing, supervision, project administration.

Conflicts of interest

There are no conflicts to declare.

Acknowledgements

We gratefully acknowledge the financial support provided by the National Natural Science Foundation of China under Grant No. 22376018. In addition, the authors were grateful for the support from the open research fund for large-scale scientific instruments of Dalian University of Technology.

Notes and references

1 A. Allman, P. Daoutidis, W. A. Arnold and E. L. Cussler, Efficient water pollution abatement, *Ind. Eng. Chem. Res.*, 2019, **58**, 22483–22487.
2 Y. Li, J. Pang and X. H. Bu, Multi-functional metal-organic frameworks for detection and removal of water pollution, *Chem. Commun.*, 2022, **58**, 7890–7908.
3 A. Trajanov, V. Kuzmanovski, B. Real, J. M. Perreau, S. Džeroski and M. Debeljak, Modeling the risk of water pollution by pesticides from imbalanced data, *Environ. Sci. Pollut. Res.*, 2018, **25**, 18781–18792.
4 K. N. Heck, S. Garcia-Segura, P. Westerhoff and M. S. Wong, Catalytic converters for water treatment, *Acc. Chem. Res.*, 2019, **52**, 906–915.
5 M. Zhan, M. You, L. Liu, Y. Zhang, F. Yuan, B. Guo, G. Cheng and W. Xu, Numerical simulation of mechanical flocculation in water treatment, *J. Environ. Chem. Eng.*, 2021, **9**, 105536.
6 Y. Liu, J. Ma, L. Lian, X. Wang, H. Zhang, W. Gao and D. Lou, Flocculation performance of alginate grafted polysilicate aluminum calcium in drinking water treatment, *Process Saf. Environ. Prot.*, 2021, **155**, 287–294.
7 V. I. Parvulescu, F. Epron, H. Garcia and P. Granger, Recent Progress and Prospects in Catalytic Water Treatment, *Chem. Rev.*, 2022, **122**, 2981–3121.
8 J. Cai, J. Huang, S. Wang, J. Iocozzia, Z. Sun, J. Sun, Y. Yang, Y. Lai and Z. Lin, Crafting Mussel-Inspired Metal Nanoparticle-Decorated Ultrathin Graphitic Carbon Nitride for the Degradation of Chemical Pollutants and Production of Chemical Resources, *Adv. Mater.*, 2019, **31**, 1806314.
9 T. Cai, Y. Liu, L. Wang, W. Dong and G. Zeng, Recent advances in round-the-clock photocatalytic system: Mechanisms, characterization techniques and applications, *J. Photochem. Photobiol., C*, 2019, **39**, 58–75.
10 J. Y. Y. Loh, N. P. Kherani and G. A. Ozin, Persistent CO_2 photocatalysis for solar fuels in the dark, *Nat. Sustain.*, 2021, **4**, 466–473.
11 J. Wei, X. Jiao, T. Wang and D. Chen, Fast, simultaneous metal reduction/deposition on electrospun a-WO_3/PAN nanofiber membranes and their potential applications for water purification and noble metal recovery, *J. Mater. Chem. A*, 2018, **6**, 14577–14586.
12 C. Zhang, Y. Li, M. Li, D. Shuai, X. Zhou, X. Xiong, C. Wang and Q. Hu, Continuous photocatalysis via photo-charging and dark-discharging for sustainable environmental remediation: Performance, mechanism, and influencing factors, *J. Hazard. Mater.*, 2021, **420**, 126607.
13 L. Wang, J. Zhang, Y. Zhang, H. Yu, Y. Qu and J. Yu, Inorganic Metal-Oxide Photocatalyst for H_2O_2 Production, *Small*, 2022, **18**, e2104561.
14 Y. Sun, L. Han and P. Strasser, A comparative perspective of electrochemical and photochemical approaches for catalytic H_2O_2 production, *Chem. Soc. Rev.*, 2020, **49**, 6605–6631.
15 W. Yu, C. Hu, L. Bai, N. Tian, Y. Zhang and H. Huang, Photocatalytic hydrogen peroxide evolution: What is the most effective strategy?, *Nano Energy*, 2022, **104**, 107906.
16 Y. Lu, G. Liu, J. Zhang, Z. Feng, C. Li and Z. Li, Fabrication of a monoclinic/hexagonal junction in WO_3 and its enhanced photocatalytic degradation of rhodamine B, *Chin. J. Catal.*, 2016, **37**, 349–358.
17 L. Zhi, S. Zhang, Y. Xu, J. Tu, M. Li, D. Hu and J. Liu, Controlled growth of AgI nanoparticles on hollow WO_3 hierarchical structures to act as Z-scheme photocatalyst for visible-light photocatalysis, *J. Colloid Interface Sci.*, 2020, **579**, 754–765.
18 Y. Wang, Y. Wang, J. Zhao and Y. Xu, Effect of inorganic ions on H_2O_2 production over illuminated Au/WO_3 with visible light, *Appl. Catal., B*, 2021, **299**, 120676.
19 Y. Wang, Y. Wang, J. Zhao, M. Chen, X. Huang and Y. Xu, Efficient production of H_2O_2 on Au/WO_3 under visible light and the influencing factors, *Appl. Catal., B*, 2021, **284**, 119691.
20 P. Xia, X. Pan, S. Jiang, J. Yu, B. He, P. M. Ismail, W. Bai, J. Yang, L. Yang, H. Zhang, M. Cheng, H. Li, Q. Zhang, C. Xiao and Y. Xie, Designing a redox heterojunction for photocatalytic "overall nitrogen fixation" under mild conditions, *Adv. Mater.*, 2022, **34**, e2200563.
21 H. Jiang, J. J. Hong, X. Wu, T. W. Surta, Y. Qi, S. Dong, Z. Li, D. P. Leonard, J. J. Holoubek, J. C. Wong, J. J. Razink, X. Zhang and X. Ji, Insights on the Proton Insertion Mechanism in the Electrode of Hexagonal Tungsten Oxide Hydrate, *J. Am. Chem. Soc.*, 2018, **140**, 11556–11559.
22 L. Zheng, M. Zhou, Z. Huang, Y. Chen, J. Gao, Z. Ma, J. Chen and X. Tang, Self-protection mechanism of hexagonal WO_3-based $DeNO_x$ catalysts against alkali poisoning, *Environ. Sci. Technol.*, 2016, **50**, 11951–11956.
23 W. Sun, M. T. Yeung, A. T. Lech, C. W. Lin, C. Lee, T. Li, X. Duan, J. Zhou and R. B. Kaner, High surface area tunnels in hexagonal WO_3, *Nano Lett.*, 2015, **15**, 4834–4838.
24 J. Yang, X. Chen, X. Liu, Y. Cao, J. Huang, Y. Li and F. Liu, From hexagonal to monoclinic: Engineering crystalline phase to boost the intrinsic catalytic activity of tungsten oxides for the hydrogen evolution reaction, *ACS Sustain. Chem. Eng.*, 2021, **9**, 5642–5650.
25 H. Yang, Z.-C. Zhao, Y.-P. Yang, Z. Zhang, W. Chen, R.-Q. Yan, Y. Jin and J. Zhang, Defective WO_3 nanoplates controllably decorated with MIL-101(Fe) nanoparticles to

efficiently remove tetracycline hydrochloride by S-scheme mechanism, *Sep. Purif. Technol.*, 2022, **300**, 121846.
26 Z. Yousaf, S. Sajjad, S. A. K. Leghari, S. Noor, A. Kanwal, S. H. Bhatti, K. H. Mahmoud and Z. M. El-Bahy, Influence of integrated nitrogen functionalities in nitrogen doped graphene modified WO_3 functional visible photocatalyst, *J. Environ. Chem. Eng.*, 2021, **9**, 106746.
27 Y. Zhang, Y. Chen, X. Wang, Y. Feng, H. Zhang and G. Zhang, Self-polarization triggered multiple polar units toward electrochemical reduction of CO_2 to ethanol with high selectivity, *Angew. Chem., Int. Ed.*, 2023, **62**, e202302241.
28 X. Chen, R. Huang, M. Ding, H. He, F. Wang and S. Yin, Hexagonal WO_3/3D porous graphene as a novel zinc intercalation anode for aqueous zinc-ion batteries, *ACS Appl. Mater. Interfaces*, 2022, **14**, 3961–3969.
29 Y. Lu, J. Zhang, F. Wang, X. Chen, Z. Feng and C. Li, K_2SO_4-assisted hexagonal/monoclinic WO_3 phase junction for efficient photocatalytic degradation of RhB, *ACS Appl. Energy Mater.*, 2018, **1**, 2067–2077.
30 H. Li, C. J. Firby and A. Y. Elezzabi, Rechargeable aqueous hybrid Zn^{2+}/Al^{3+} electrochromic batteries, *Joule*, 2019, **3**, 2268–2278.
31 J. Wei, X. Jiao, T. Wang and D. Chen, The fast and reversible intrinsic photochromic response of hydrated tungsten oxide nanosheets, *J. Mater. Chem. C*, 2015, **3**, 7597–7603.
32 J. Wei, X. Jiao, T. Wang and D. Chen, Electrospun photochromic hybrid membranes for flexible rewritable media, *ACS Appl. Mater. Interfaces*, 2016, **8**, 29713–29720.
33 D. Li, J. Wei, S. Dong, H. Li, Y. Xia, X. Jiao, T. Wang and D. Chen, Novel PVP/HTA hybrids for multifunctional rewritable paper, *ACS Appl. Mater. Interfaces*, 2018, **10**, 1701–1706.
34 X. Dong, Z. Wu, Y. Guo, Y. Tong, X. Liu, L. Zhang and Y. Lu, Rational modification in the photochromic and self-bleaching performance of hierarchical microsphere Cu@h-WO_3/$WO_3 \cdot nH_2O$ composites, *Sol. Energy Mater. Sol. Cells*, 2021, **219**, 110784.
35 S. Songara, V. Gupta, M. Kumar Patra, J. Singh, L. Saini, G. Siddaramana Gowd, S. Raj Vadera and N. Kumar, Tuning of crystal phase structure in hydrated WO_3 nanoparticles under wet chemical conditions and studies on their photochromic properties, *J. Phys. Chem. Solids*, 2012, **73**, 851–857.
36 I. M. Szilágyi, B. Fórizs, O. Rosseler, Á. Szegedi, P. Németh, P. Király, G. Tárkányi, B. Vajna, K. Varga-Josepovits, K. László, A. L. Tóth, P. Baranyai and M. Leskelä, WO_3 photocatalysts: Influence of structure and composition, *J. Catal.*, 2012, **294**, 119–127.
37 Y. Hosakun, K. Halász, M. Horváth, L. Csóka and V. Djoković, ATR-FTIR study of the interaction of CO_2 with bacterial cellulose-based membranes, *Chem. Eng. J.*, 2017, **324**, 83–92.
38 F. Yang, F. Wang and Z. Guo, Characteristics of binary WO_3@CuO and ternary WO_3@PDA@CuO based on impressive sensing acetone odor, *J. Colloid Interface Sci.*, 2018, **524**, 32–41.
39 Z. Wu, J. Shen, W. Li, J. Li, D. Xia, D. Xu, S. Zhang and Y. Zhu, Electron self-sufficient core-shell BiOCl@Fe-BiOCl nanosheets boosting Fe (III)/Fe (II) recycling and synergetic photocatalysis-Fenton for enhanced degradation of phenol, *Appl. Catal., B*, 2023, **330**, 122642.
40 H. Liu, F. Zhang, H. Wang, J. Xue, Y. Guo, Q. Qian and G. Zhang, Oxygen vacancy engineered unsaturated coordination in cobalt carbonate hydroxide nanowires enables highly selective photocatalytic CO_2 reduction, *Energy Environ. Sci.*, 2021, **14**, 5339–5346.
41 H. Liu, Y. Chen, H. Li, G. Wan, Y. Feng, W. Wang, C. Xiao, G. Zhang and Y. Xie, Construction of asymmetrical dual Jahn–Teller sites for photocatalytic CO_2 reduction, *Angew. Chem., Int. Ed.*, 2023, **62**, e202304562.
42 X. L. Wu, S. Liu, Y. Li, M. Yan, H. Lin, J. Chen, S. Liu, S. Wang and X. Duan, Directional and Ultrafast Charge Transfer in Oxygen-Vacancy-Rich ZnO@Single-Atom Cobalt Core-Shell Junction for Photo-Fenton-Like Reaction, *Angew. Chem., Int. Ed.*, 2023, **62**, e202305639.
43 X. Sun, L. Li, S. Jin, W. Shao, H. Wang, X. Zhang and Y. Xie, Interface boosted highly efficient selective photooxidation in Bi_3O_4Br/Bi_2O_3 heterojunctions, *eScience*, 2023, **3**, 100095.
44 S. Zhang, J. Chen, W.-S. Yang and X. Chen, Vacancies-rich CoAl monolayer layered double hydroxide as efficient superoxide dismutase-like nanozyme, *Nano Res.*, 2022, **15**, 7940–7950.
45 Y. Li, J. Chen, Y. Ji, Z. Zhao, W. Cui, X. Sang, Y. Cheng, B. Yang, Z. Li, Q. Zhang, L. Lei, Z. Wen, L. Dai and Y. Hou, Single-atom Iron Catalyst with Biomimetic Active Center to Accelerate Proton Spillover for Medical-level Electrosynthesis of H_2O_2 Disinfectant, *Angew. Chem., Int. Ed.*, 2023, **62**, e202306491.
46 F. Meng, Y. Wang, Z. Chen, J. Hu, G. Lu and W. Ma, Synthesis of CQDs@FeOOH nanoneedles with abundant active edges for efficient electro-catalytic degradation of levofloxacin: Degradation mechanism and toxicity assessment, *Appl. Catal., B*, 2021, **282**, 119597.
47 D. Meyerstein, Re-examining Fenton and Fenton-like reactions, *Nat. Rev. Chem*, 2021, **5**, 595–597.
48 J. Lin, W. Tian, Z. Guan, H. Zhang, X. Duan, H. Wang, H. Sun, Y. Fang, Y. Huang and S. Wang, Functional Carbon Nitride Materials in Photo-Fenton-Like Catalysis for Environmental Remediation, *Adv. Funct. Mater.*, 2022, **32**, 2201743.
49 J. Xu, X. Zheng, Z. Feng, Z. Lu, Z. Zhang, W. Huang, Y. Li, D. Vuckovic, Y. Li, S. Dai, G. Chen, K. Wang, H. Wang, J. K. Chen, W. Mitch and Y. Cui, Organic wastewater treatment by a single-atom catalyst and electrolytically produced H_2O_2, *Nat. Sustain.*, 2020, **4**, 233–241.
50 Y. Nosaka and A. Y. Nosaka, Generation and detection of reactive oxygen species in photocatalysis, *Chem. Rev.*, 2017, **117**, 11302–11336.
51 H. Huang, H.-L. Wang, S.-B. Shi and W.-F. Jiang, In-situ fabrication of $AgI/Ag_nMo_xO_{3x+n/2}$/g-C_3N_4 ternary composite photocatalysts for benzotriazole degradation: Tuning the heterostructure, photocatalytic activity and photostability

by the degree of molybdate polymerization, *Sep. Purif. Technol.*, 2023, **307**, 122874.

52 H. Huang, H. L. Wang and W. F. Jiang, In-situ synthesis of novel dual S-scheme $AgI/Ag_6Mo_7O_{24}/g\text{-}C_3N_4$ heterojunctions with tandem structure for photocatalytic degradation of organic pollutants, *Chemosphere*, 2023, **318**, 137812.

53 Y. Sun, D. Wang and Y. Zhu, Deep degradation of pollutants by perylene diimide supramolecular photocatalyst with unique Bi-planar π–π conjugation, *Chem. Eng. J.*, 2022, **438**, 135667.

54 J. Wang, X. Zhou, J. Hao, Z. Wang, B. Huo, J. Qi, Y. Wang and F. Meng, Sustainable self-powered degradation of antibiotics using $Fe_3O_4@MoS_2$/PVDF modified pipe with superior piezoelectric activity: Mechanism insight, toxicity assessment and energy consumption, *Appl. Catal., B*, 2023, **331**, 122655.

55 X. Mao, M. Wang, J. Li, M. Zhang, C. Dong, H. Lei, Y. He, M. Zhang, Z. Ge, R. Shen, H. Han, J. Hu and G. Wu, High atom utility of robust Ca-Co bimetallic catalyst for efficient Fenton-like catalysis in advanced oxidation processes, *Appl. Catal., B*, 2023, **331**, 122698.

56 Y. Chen, L. Liu, L. Zhang, S. Li, X. Zhang, W. Yu, F. Wang, W. Xue, H. Wang and Z. Bian, Construction of Z-type heterojunction $BiVO_4/Sm/\alpha\text{-}Fe_2O_3$ photoanode for selective degradation: Efficient removal of bisphenol A based on multifunctional Sm-doped modification, *Appl. Catal., B*, 2023, **333**, 122775.

57 B. Wang, Z. Li, H. Ma, J. Zhang, L. Jiao, H. Hao, E. Liu, L. Xu, C. Wang, B. Zhou and X. Ma, Dynamic construction of self-assembled supramolecular H_{12}SubPcB-OPhCOOH/Ag_3PO_4 S-scheme arrays for visible photocatalytic oxidation of antibiotics, *Appl. Catal., B*, 2022, **318**, 121882.

58 Y. Zhang, Y. Li and Y. Yuan, Carbon quantum dot-decorated $BiOBr/Bi_2WO_6$ photocatalytic micromotor for environmental remediation and DFT calculation, *ACS Catal.*, 2022, **12**, 13897–13909.

59 Y. Cheng, J. Chen, P. Wang, W. Liu, H. Che, X. Gao, B. Liu and Y. Ao, Interfacial engineering boosting the piezocatalytic performance of Z-scheme heterojunction for carbamazepine degradation: Mechanism, degradation pathway and DFT calculation, *Appl. Catal., B*, 2022, **317**, 121793.

60 S. Zhang, G. Hu, M. Chen, B. Li, W. Dai, F. Deng, L. Yang, J. Zou and S. Luo, Interfacial oxygen vacancy modulated $Ag_3PO_4@MoS_2$ Z-scheme system for efficient photocatalytic hydrogen recovery from antibiotic wastewater, *Appl. Catal., B*, 2023, **330**, 122584.

61 Z. Zhang, J. Liang, W. Zhang, M. Zhou, X. Zhu, Z. Liu, Y. Li, Z. Guan, C.-S. Lee, P. K. Wong, H. Li and Z. Jiang, Modified-pollen confined hybrid system: A promising union for visible-light-driven photocatalytic antibiotic degradation, *Appl. Catal., B*, 2023, **330**, 122621.